# Complete inverse design to customize two-dimensional dispersion relation via nonlocal phononic crystals

Sharat Paul, Md Nahid Hasan, Henry Chien Fu,* and Pai Wang†
*Department of Mechanical Engineering, University of Utah, Salt Lake City, Utah 84112, USA*

(Received 14 June 2024; revised 3 September 2024; accepted 23 September 2024; published 11 October 2024)

We report a new method to tailor the entire two-dimensional (2D) dispersion relation based on nonlocal phononic crystals, where beyond-nearest-neighbor (BNN) interactions are used to achieve precise sculpting of the band surface. Focusing on square lattices, we demonstrate unconventional band structures such as multifold symmetries, roton/maxon/saddle-type critical points, anisotropy-to-isotropy transitions, and other exotic band morphologies. We anticipate that the design protocols in this study can be extended to all other two-dimensional lattices and multiband customization.

DOI: 10.1103/PhysRevB.110.144304

## I. INTRODUCTION

Phononic metamaterials manipulate wave propagation beyond the capabilities of natural materials [1–4]. They have wide applications in noise reduction [5,6], energy harvesting [7–9], and wave guiding [10–13] due to their unprecedented capability to control wave propagation. Recent developments in phononic metamaterials include geometric phase effects [14,15], anharmonic response [16], localized modes [17–20], frozen evanescent waves [21], band-gap engineering [22–26], wave-number band gap [27], phononic topology [28], and the study of snake states [29].

The dispersion relation is the central theme in this research area since it describes how frequency depends on wave vectors [30,31]. Customizing the dispersion relation can create novel wave behaviors [32–34]. However, most metamaterials with local interactions may manifest monotonic dispersion bands only. Therefore, there are considerable limitations in our ability to solve the inverse problem: Designing the lattice structures from given target dispersion bands. In contrast, incorporating beyond-nearest-neighbor (BNN) interactions, nonlocal [35–37] metamaterials may achieve more exotic wave phenomena [38,39], such as diffusive transport [40], active control [7], maxonlike [41,42] and rotonlike properties [43–49], reflection/transmission behavior [50], as well as extreme spatial dispersion [51]. All these properties were achieved by focusing on the forward process and finding wave behaviors from specific structures. A recent breakthrough [32] on one-dimensional metamaterials showed the possibility of inverse design to achieve any valid dispersion curves. However, the inverse design of two-dimensional metamaterials, particularly for customizing dispersion relations, remains an uncharted research area.

In this paper, we show the inverse design of two-dimensional (2D) phononic crystals using BNN interactions to customize dispersion relations. We address the inverse problem, enabling precise engineering of single-band dispersion in two-dimensional monoatomic lattices for scalar-wave [52–54] propagation. Furthermore, we apply the inverse design process to several target dispersions, achieving band structures of different symmetry groups, maxon/roton/saddle points, anisotropy-to-isotropy transitions [55–58], and other exotic 2D surface morphologies. Our method can accommodate both analytical expressions and numerical data as target dispersion surfaces. Although we exclusively focus on the square lattice in this paper, the same method can be applied to all two-dimensional lattices, enabling a myriad of directions of future research. Our results contribute to fundamental knowledge about the design and fabrication of advanced metamaterials by enhancing our understanding of wave-material interactions.

## II. 2D NONLOCAL PHONONIC CRYSTALS

We start with a two-dimensional monoatomic square lattice with identical masses $m$, illustrated as blue spheres in Fig. 1. Linear springs, depicted as solid lines in Figs. 1(b)–1(d), connect each mass to its $(n_x, n_y)$th neighbor, where $n_x, n_y \leqslant N$, where the upper bound $N$ indicates the lattice complexity of the design. Neglecting the "self-connection" case of $(n_x, n_y) = (0, 0)$, we count that every lattice site has a total of $(2N + 1)^2 - 1$ connections with other sites. The well-known local square lattice and the primary nonlocal interactions are shown in Figs. 1(b) and 1(c), respectively. Figure 1(d) shows some examples of longer-range nonlocal interactions with red lines for $(n_x, n_y) = (\pm 2, 0)$ and $(0, \pm 2)$ as well as green lines for $(n_x, n_y) = (\pm 1, \pm 3)$. Applying Bloch's theorem and solving the equations of motion, we derive the dispersion relation of the two-dimensional monoatomic lattice (see Secs. I A and I B of Supplemental Materials [59] for details) as

$$\omega^2(q_x, q_y) = \frac{2}{m}(K^+ + K^-), \tag{1}$$

*Contact author: henry.fu@utah.edu
†Contact author: pai.wang@utah.edu

 

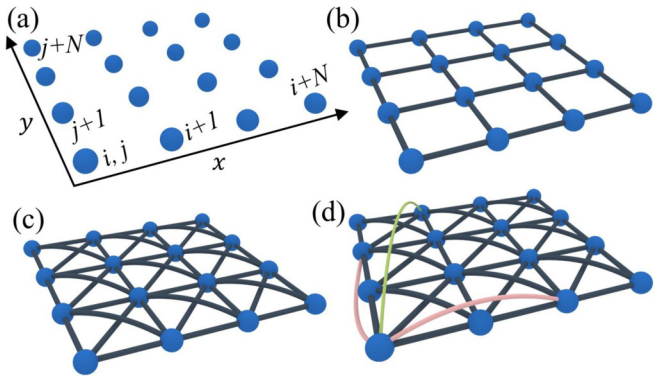


FIG. 1. Schematics of the 2D square lattice for local and nonlocal phononic crystals. (a) Arrangement of lattice points (blue spheres) along the $x$ and $y$ axes. (b) Square lattice with local connections only. The black lines represent linear springs. (c) Addition of some nonlocal stiffness. (d) Illustration of more nonlocal interactions within the lattice. The red and green springs are shown only for one mass for clear visualization.

where

$$K^{\pm} = \sum_{n_x=0}^{N} \sum_{n_y=0}^{N} \gamma k_{\pm n_x, n_y} [1 - \cos(Q_x \pm Q_y)], \tag{2}$$

$$\gamma = \begin{cases} \frac{1}{2}, & n_x n_y = 0 \\ 1, & \text{otherwise.} \end{cases} \tag{3}$$

Here, $\omega$ denotes the frequency, while $(q_x, q_y)$ represents the wave vector, and we have

$$Q_x = n_x a_x q_x \quad \text{and} \quad Q_y = n_y a_y q_y, \tag{4}$$

where $a_x$ and $a_y$ are the lattice constants. In this context, $k_{n_x,n_y}$ characterizes the stiffness between any mass and its $(n_x, n_y)$th neighbor, and we set $k_{0,0} = 0$. We note that, due to the periodic nature of the lattice, the following always hold:

$$k_{n_x,n_y} = k_{-n_x,-n_y} \quad \text{and} \quad k_{-n_x,n_y} = k_{n_x,-n_y}. \tag{5}$$

## III. CONDITIONS FOR VALID TARGETS

Without any active or gyroscopic components in the design, the dispersion must satisfy the *reciprocity* condition, which ensures the parity symmetry in the 2D wave-vector space:

$$\omega(q_x, q_y) = \omega(-q_x, -q_y). \tag{6}$$

This guarantees that the dispersion surface is at least twofold rotational symmetric. In addition, *Hermiticity*, *passivity*, and *periodicity* dictate that the dispersion must satisfy the following:

$$\begin{aligned} \omega &= 0, \quad (q_x, q_y) = (0, 0) \\ \omega &> 0, \quad (q_x, q_y) \neq (0, 0) \\ \partial\omega/\partial q_x &= 0, \quad q_x = \pm\pi/a_x \\ \partial\omega/\partial q_y &= 0, \quad q_y = \pm\pi/a_y. \end{aligned} \tag{7}$$

Lastly, we need the target dispersion to be a *smooth* surface defined over the first Brillouin zone (BZ) so that the wave-group velocity is well defined for all possible wave vectors. All conditions for a valid dispersion relation are described in detail in Sec. I C of Supplemental Materials [59]. Additionally, we do not consider any damping and nonlinear wave dynamics in the system and the lattice size is infinite.

## IV. INVERSE DESIGN

The dispersion relation in Eq. (1) resembles a two-dimensional Fourier cosine series, which enables the precise tailoring. Given any valid 2D dispersion surface $\Omega(q_x, q_y)$ as the target, we first calculate the following integrals over the first Brillouin zone (see Sec. I D of Supplemental Materials for detail [59]):

$$A_{xy} = \frac{a_x a_y}{\pi^2} \iint_{\mathrm{BZ}} \Omega^2 \cos(Q_x + Q_y)\, \mathrm{d}q_x \mathrm{d}q_y, \tag{8}$$

$$B_{xy} = \frac{a_x a_y}{\pi^2} \iint_{\mathrm{BZ}} \Omega^2 \cos(Q_x - Q_y)\, \mathrm{d}q_x \mathrm{d}q_y. \tag{9}$$

Next, we numerically integrate Eqs. (8) and (9) and obtain the spring stiffness as necessary design variables

$$k_{n_x,n_y} = k_{-n_x,-n_y} = -mA_{xy}/(2\gamma), \tag{10}$$

$$k_{-n_x,n_y} = k_{n_x,-n_y} = -mB_{xy}/(2\gamma). \tag{11}$$

Applying the Fourier theory to two-dimensional space, we note that $\sin(Q_x \pm Q_y)$ and $\cos(Q_x \pm Q_y)$ for $n_x, n_y = 1, 2, \ldots$ form a complete and orthogonal basis for all smooth periodic functions. However, any Fourier series comprising $\sin(Q_x \pm Q_y)$ terms will not satisfy the validity conditions of parity symmetry in Eq. (6). Thus, we confirm that our approach can in principle achieve any valid dispersion surface.

To demonstrate the inverse design, we use target dispersion bands defined by either closed-form analytical expressions or arrays of numerical points. For this study, we standardize the unit mass ($m = 1$) and lattice constants ($a_x = a_y = 1$) in Eq. (1) for the square lattice. The remaining design variables are $k_{n_x,n_y}$ and $k_{-n_x,n_y}$ stiffness values. We set a limit on the longest-range interaction as $N = 30$, allowing a maximum of 3720 connections at each mass, among which 4 are local, while 3716 are BNN interactions. Because of Eq. (5), the total number of design variables is $2(N^2 + N) = 1860$. We perform this inverse design for ten different target dispersions and present them as case I through case X in the remaining part of this paper. Furthermore, across all cases, we evaluate the normalized root-mean-square deviation (NRMSD) of the achieved dispersion from the target surface to ensure consistent comparisons:

$$\mathrm{NRMSD} = \sqrt{\frac{1}{T} \sum_{q_x,q_y} \left( \frac{\Omega(q_x, q_y) - \omega(q_x, q_y)}{\Omega_{\max}} \right)^2}, \tag{12}$$

where the summation is taken over the first Brillouin zone. $\Omega(q_x, q_y)$ and $\omega(q_x, q_y)$ denote the target and achieved dispersion bands, respectively, while $T$ is the total number of sampling points we use in the wave-vector space. We normalize both dispersions using the maximum frequency of the

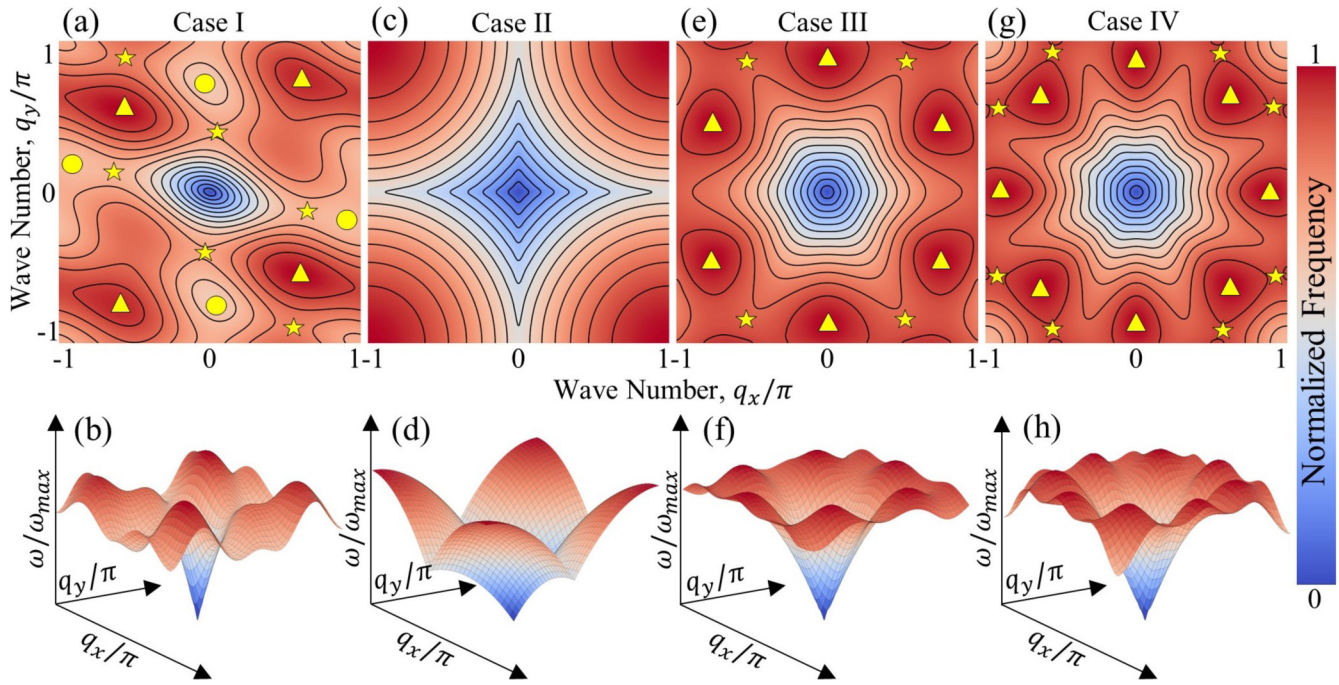


FIG. 2. Demonstration of dispersion relations exhibiting $n$-fold rotational symmetries (i.e., $C_n$) within the BZ. Here, (a) and (c) display the contour of dispersion relations with perfect $C_2$ and $C_4$ symmetry, respectively, illustrating the fundamental bidirectional and quadrilateral symmetry inherent to the square lattice structure and their 3D views within the BZ are shown in (b) and (d). Furthermore, (e) and (g) present nearly $C_6$ and $C_8$ symmetry, respectively, within a circular region of radius $\pi$ and the center at (0, 0) wave number while (f) and (h) display 3D views of the corresponding dispersion. The yellow-marked triangle, circle, and star shapes represent maxon, roton, and saddle points, respectively.

target, $\Omega_{\max}$ (see Sec. I E of Supplemental Materials [59] for detail).

## V. DISPERSION BANDS WITH MULTIFOLD SYMMETRIES

We investigate the possibility of achieving dispersion surfaces with rotational symmetries, labeled as $C_n$ for the cyclic group of order $n$, over the wave-vector space. While the time-reversal symmetry guarantees $C_2$ [60], the square lattice also allows us to perfectly achieve $C_4$, reflecting the square nature inherent to the lattice configuration. Furthermore, we show examples of nearly perfect $C_6$ and $C_8$ symmetries of the band structures within the region with a radius of $\pi$ from the center of the first Brillouin zone. To achieve these target dispersions for the 2D square lattice, we use Eqs. (8) and (9) to compute the stiffness values $k_{n_x,n_y}$ and $k_{-n_x,n_y}$. Figures 2(a) and 2(b) display the achieved dispersion relation with $C_2$ symmetry (case I). The target dispersion is defined analytically as

$$\Omega^2(q_x, q_y) = \tfrac{1}{2}[5 - \cos(q_x) - \cos(q_y) - \cos(2q_x) - \cos(2q_y) - \cos(q_x + 3q_y)], \quad (13)$$

which is obtained directly from Eq. (1) and the lattice structure is shown in Fig. 1(d) considering $k_{\pm1,1} = 0$. The rationale behind targeting the dispersion of a known lattice is to evaluate the efficacy of our inverse design method in achieving a lattice structure that is either identical or reasonably close to the known one. We find that the NRMSD is negligible with $N \geqslant 3$ for this case I, indicating a good performance of the customization procedure. As our customization achieves exact lattice structure for case I, we exclude the error analysis in this case. This allows us to proceed to more arbitrarily defined target dispersion surfaces.

Figures 2(c) and 2(d) show the achieved dispersion relations with $C_4$ symmetry (case II) and the target equation as

$$\Omega(q_x, q_y) = -(|q_x| - \pi)^2 - (|q_y| - \pi)^2 + 2\pi^2, \quad (14)$$

which has the semi-spherical geometry of radius $\pi$. Here, we obtain NRMSD $\leqslant 2\%$ for $N = 3$, NRMSD $\leqslant 1\%$ for $N = 5$, and NRMSD $\leqslant 0.1\%$ for $N = 22$. In addition, we achieve NRMSD $= 0.06\%$ with $N = 30$, in which case only 224 out of 3716 BNN interactions have normalized stiffness $|k_{\pm n_x,n_y}/k^*| > 0.001$, where $k^*$ denotes the stiffness with maximum absolute value in the lattice.

Given the inherent limitations of the square lattice, which preclude perfect symmetries beyond $C_4$, we show nearly perfect $C_6$ and $C_8$ symmetric dispersion bands within the square lattice. Here, without using analytically defined targets such as Eqs. (13) and (14), we instead use a 2D array of numerically generated data (see Sec. I F of Supplemental Materials [59] for detail) on the uniform grid of $1000\times1000$ points over the first Brillouin zone as the target dispersion for the inverse design. Figures 2(e) and 2(f) illustrate the achieved dispersion showing nearly $C_6$ symmetry (case III). This dispersion is achieved with $N = 4$ lattice structure maintaining an NRMSD $\leqslant 1\%$. Furthermore, we obtain NRMSD $\leqslant 0.1\%$ for $N = 16$, where 404 out of 3716 BNN connections have normalized stiffness values greater than 0.001. Additionally, Figs. 2(g)

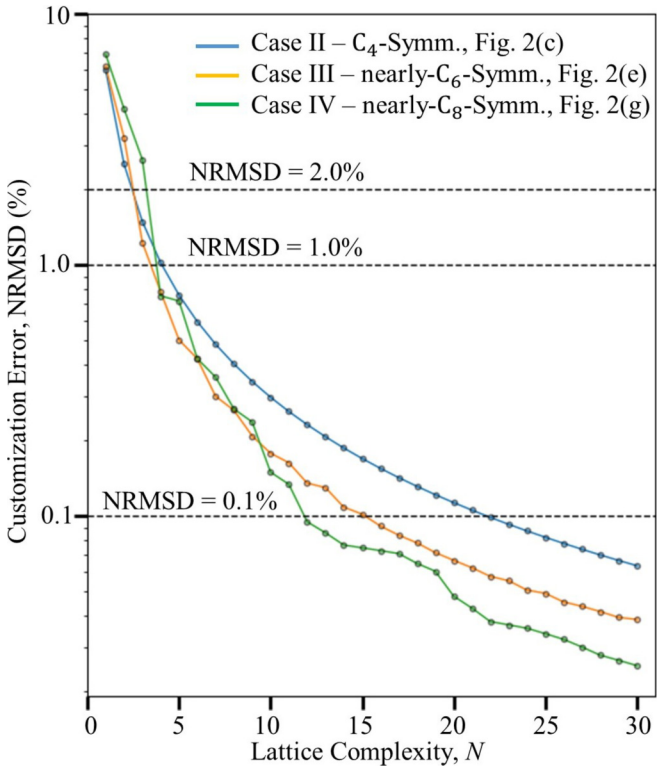


FIG. 3. Error analyses for cases II, III, and IV dispersion relations shown in Figs. 2(c), 2(e), and 2(g), respectively, indicating the lattice complexity needed to achieve 2%, 1%, and 0.1% NRMSD.

and 2(h) present the nearly $C_8$ symmetric (case IV) achieved dispersion surface. Our results show that a lattice of $N = 30$ can realize case IV dispersion with NRMSD $\leqslant 0.025\%$ and only 98 BNN interactions have normalized stiffness higher than the threshold we set. We also find NRMSD $\leqslant 1\%$ for $N = 4$ and NRMSD $\leqslant 0.1\%$ for $N = 12$.

We calculate the errors between the target and achieved dispersions using Eq. (12) and provide the error-analysis plots in Fig. 3 for cases II, III, and IV presented in Figs. 2(c)–2(h). The results indicate that complex lattices with larger $N$ perform better. If aiming at NRMSD $\leqslant 2\%$, we can use less complex designs with $N = 4$. In contrast, achieving NRMSD $\leqslant 0.1\%$ would necessitate more complex designs with $N > 12$. Here, we omit the error analyses of case I shown in Fig. 2(a), as we can achieve an exact match with $N = 3$ according to Eq. (13).

## VI. DISPERSION WITH CRITICAL POINTS

Next, we apply our inverse design approach to customize dispersion bands, introducing multiple localized modes [20,32,43]—maxon/roton/saddle points. These zero-group-velocity (ZGV) wave modes occur at the dispersion surface's critical points (CPs), where

$$\frac{\partial \omega}{\partial q_x} = 0 \quad \text{and} \quad \frac{\partial \omega}{\partial q_y} = 0. \tag{15}$$

For the case I dispersion in Figs. 2(a) and 2(b), we observe four maxons (triangles), four rotons (circles), and six saddle points (stars) within the BZ. Furthermore, the case III dispersion in Figs. 2(e) and 2(f) features six maxons and four saddle points. We analyze the precision of achieving these CPs by comparing their frequency and wave vector with the prescribed targets. We start with defining the CPs as M1 and M2 for maxons, as well as S for saddle point in Fig. 4(a). Due to symmetry, we can exclusively focus on the CPs in the first quadrant of BZ. Based on Eq. (15), Figs. 4(b)–4(f) represent how the CPs appear when we change the lattice complexity $N$. The CPs arise where the red curves (where $\partial\omega/\partial q_x = 0$) and blue curves (where $\partial\omega/\partial q_y = 0$) intersect. Furthermore, to categorize the CPs, we analyze the Hessian matrix of dispersion relation

$$\mathbf{H} = \begin{pmatrix} \frac{\partial^2\omega}{\partial q_x^2} & \frac{\partial^2\omega}{\partial q_x \partial q_y} \\ \frac{\partial^2\omega}{\partial q_y \partial q_x} & \frac{\partial^2\omega}{\partial q_y^2} \end{pmatrix}, \tag{16}$$

of which the determinant delineates four types of CPs as

$$\begin{aligned} &\det(\mathbf{H}) > 0 \text{ and } \partial^2\omega/\partial q_x^2 > 0, && \text{Roton} \\ &\det(\mathbf{H}) > 0 \text{ and } \partial^2\omega/\partial q_x^2 < 0, && \text{Maxon} \\ &\det(\mathbf{H}) < 0, && \text{Saddle point} \\ &\det(\mathbf{H}) = 0, && \text{Higher-order CP.} \end{aligned}$$

Note that we exclusively focus on first-order CPs (rotons, maxons, and saddle points) in this paper, while the realization of higher-order CPs [61,62] would be a worthwhile research direction for future studies. As shown in Fig. 4(b), $N = 2$ provides only one CP in each BZ quadrant, while $N = 3$ gives rise to both M1 and S in Fig. 4(c). Note that although the NRMSD $\leqslant 2\%$ for $N = 3$, still M2 doesn't appear. This manifests that the localized customization of CPs is not guaranteed by global error measures, such as the NRMSD. In contrast, all cases with $N \geqslant 4$, as shown in Figs. 4(d)–4(f), exhibit all three CPs, M1, M2, and S, in the target. We also conduct the error analysis of frequency and wave vector of the CPs and present the results in Figs. 4(g) and 4(h). We calculate the normalized differences of frequency and wave vector between the target and achieved CPs as

$$\text{Error}_\omega^{\text{CP}} = \frac{\left|\omega_{\text{T}}^{\text{CP}} - \omega_{\text{A}}^{\text{CP}}\right|}{\omega_{\text{T}}^{\text{CP}}}, \quad \text{Error}_{\mathbf{q}}^{\text{CP}} = \frac{\left\|\mathbf{q}_{\text{T}}^{\text{CP}} - \mathbf{q}_{\text{A}}^{\text{CP}}\right\|}{\left\|\mathbf{q}_{\text{T}}^{\text{CP}}\right\|}, \tag{17}$$

where $\omega_{\text{T}}^{\text{CP}}$ and $\mathbf{q}_{\text{T}}^{\text{CP}}$ indicate the frequency and wave vector, respectively, at the CPs in target dispersion. Similarly, $\omega_{\text{A}}^{\text{CP}}$ and $\mathbf{q}_{\text{A}}^{\text{CP}}$ correspond to the CPs in the achieved dispersion. We observe that $\text{Error}_\omega^{\text{CP}}$ and $\text{Error}_{\mathbf{q}}^{\text{CP}}$ remain less than 2% in Fig. 4(g) and less than 8% in Fig. 4(h), respectively, for all CPs in the case III dispersion shown in Fig. 2(e). Although the error in frequency and wave vector generally decreases with higher lattice complexity, $N$, the trend is inconsistent across all critical points discussed. However, the oscillation amplitude of the error is tiny [e.g., $\text{Error}_\omega^{\text{CP}} < 0.1\%$ for $N \geqslant 10$ and $\text{Error}_{\mathbf{q}}^{\text{CP}} < 1\%$ for $N \geqslant 5$ in Figs. 4(g) and 4(h), respectively]. Additionally, we do not specifically optimize for these discrete points; instead, we observe how the customization of the entire dispersion surface influences the accuracy at the critical points.

The case IV dispersion in Figs. 2(g) and 2(h) features eight maxons and eight saddle points. The exact locations of these CPs in the case IV target dispersion are presented in Fig. 5(a) by analyzing the first zero derivatives of $\omega$ using Eq. (15).

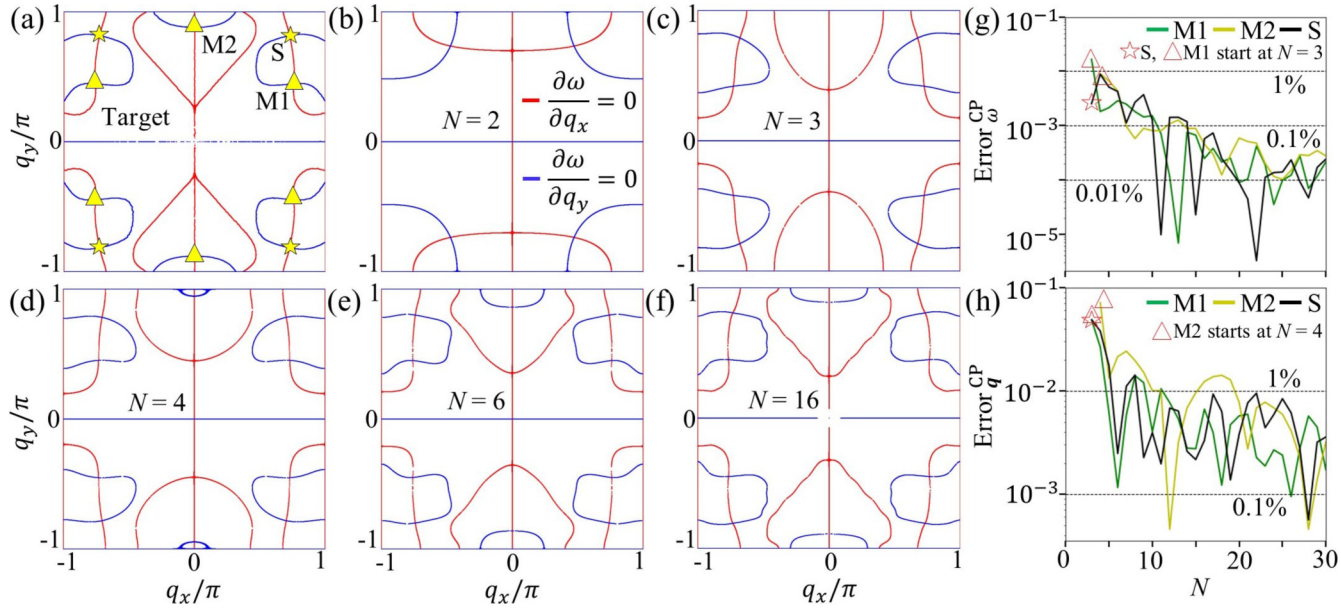


FIG. 4. Analysis of critical points in the case III dispersion relation for various $N$ values. Subfigures (a)–(f) display the first zero derivatives of $\omega$ with respect to $q_x$ and $q_y$. The derivatives $\partial\omega/\partial q_x = 0$ is shown as red lines and $\partial\omega/\partial q_y = 0$ as blue lines, with intersections indicating critical points. Here, (a) presents the CPs in target dispersion, marked with yellow triangles for maxima (M) and stars for saddle points (S) and labeled as M1, M2, and S for reference when comparing with achieved dispersion. Subsequent subfigures show CPs in achieved dispersions for (b) $N = 2$, (c) $N = 3$, (d) $N = 4$, (e) $N = 6$, and (f) $N = 16$. For $N = 2$, critical points cannot be achieved; for $N = 3$, only M1 and S are found; for $N = 4$, all M1, M2, and S appear but not at the exact wave number as the target dispersion; for $N = 6$, the wave number is very close to the target function for all critical points; and for $N = 16$, all critical points are achieved, with the entire dispersion having NRMSD $\leqslant 0.1\%$. (g) and (h) show the normalized deviance of frequency and wave number, calculated using Eq. (17), at the CPs, respectively.

We discuss the possibility of achieving 4 CPs, M1 and M2 for maxons, as well as S1 and S2 for saddle points, in the first quadrant of BZ since they represent all CPs based on the fold symmetry. Our results show that we cannot achieve all target CPs with $N = 2$ or $N = 3$, as shown in Figs. 5(b) and 5(c). In contrast, all four CPs appear for $N = 4$, Fig. 5(d), but

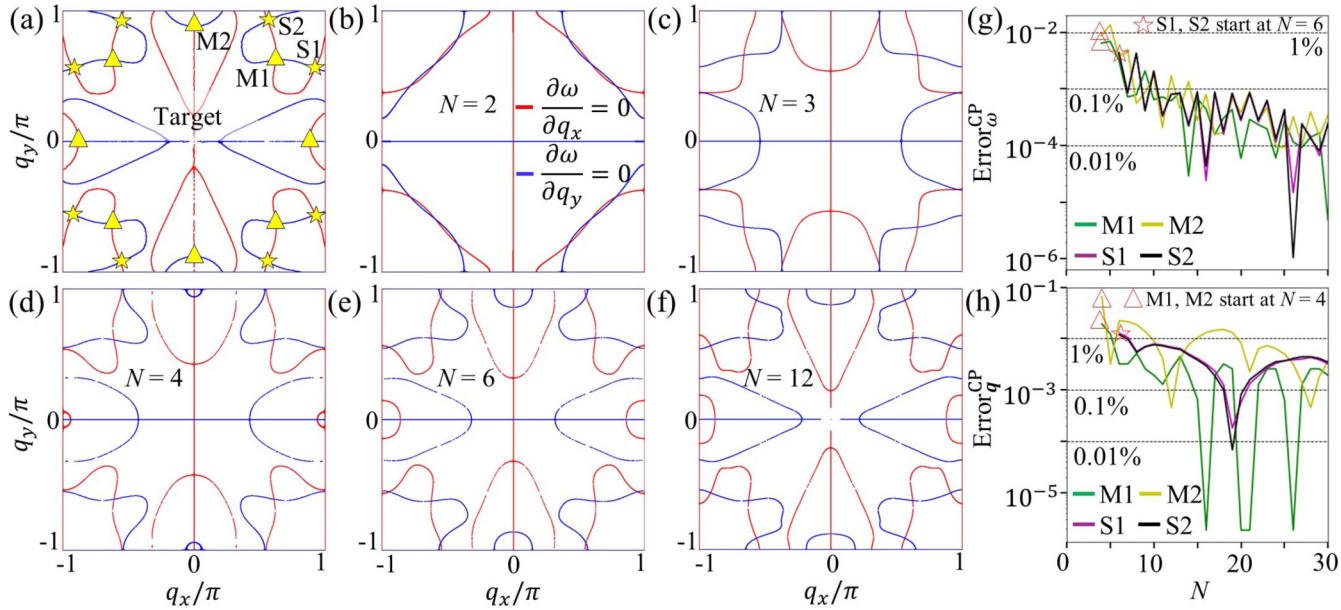


FIG. 5. Characterization of critical points in the case IV dispersion at different lattice structure. Subfigures (a)–(f) show the first derivatives of $\omega$ in the wave-vector space. (a) Shows the CPs in the target dispersion, highlighted as yellow triangle for maxon and star for saddle points. In addition, (b) $N = 2$ and (c) $N = 3$ provide only 3 CPs at each quadrant in the BZ while (d) $N = 4$ gives all the CPs in the target dispersion but they do not appear at the same location. With the increasing lattice size (e) $N = 6$, and (f) $N = 12$, the CPs get closer to the exact location in wave-vector space. Subfigures (g) and (h) present the normalized deviations of frequency and wave number, respectively, at the critical points.

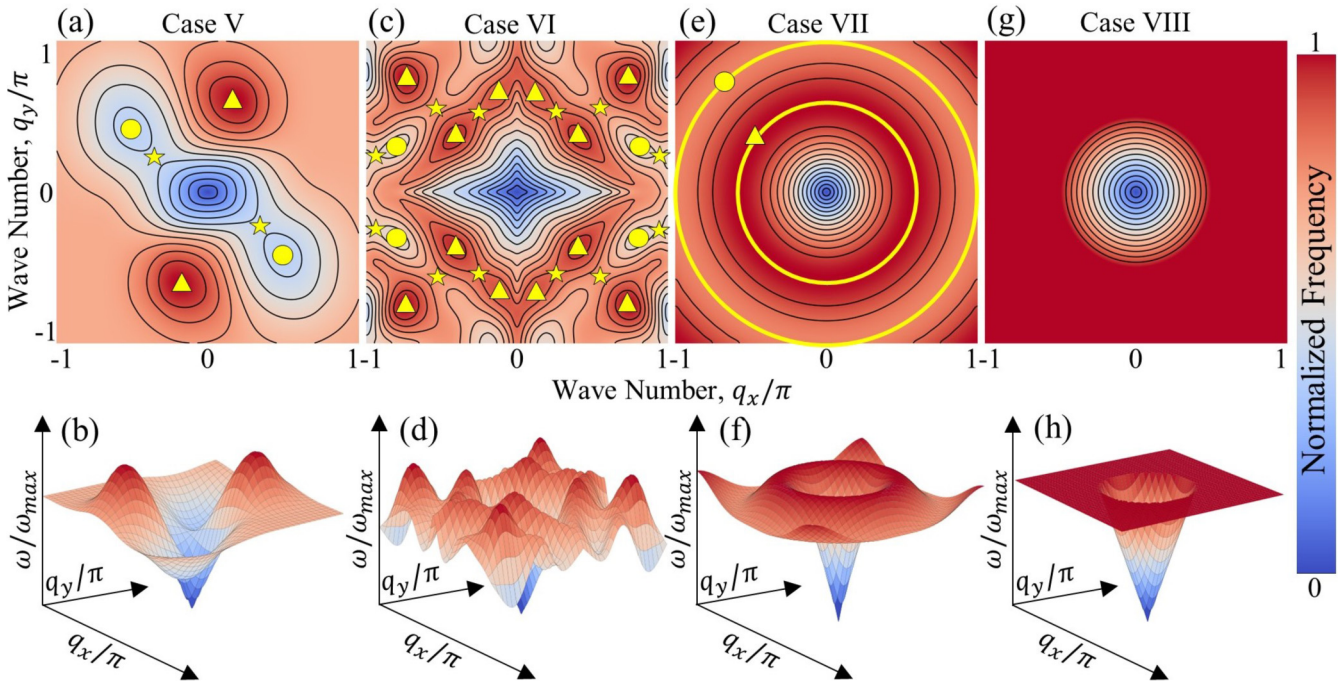


FIG. 6. Dispersion achievable in two-dimensional phononic metamaterials for various localized wave modes. Here, (a) shows a dispersion with maxon, roton, and saddle points in pair due to the time-reversal symmetry including its 3D view in (b), and (c) represents dispersion with multiple maxons, rotons, and saddle points with the 3D view in (d). Additionally, (e) displays a band featuring a ring of maxon and roton indicated by the yellow rings, and (g) shows a flat dispersion band, and their 3D views are shown in (f) and (h), respectively.

their frequencies and wave vectors remain different from the target. With larger $N$ values in Figs. 5(e) and 5(f), we find that the achieved CPs approach the target ones. We show the error analysis of CPs in Figs. 5(g) and 5(h), respectively.

Next, we note that, due to the parity symmetry, each CP must appear at least twice in the BZ. We set up a target dispersion that includes a pair of each first-order CP type: 2 rotons, 2 maxons, and 2 saddle points, as shown in Figs. 6(a) and 6(b) (case V). Our findings show that a lattice with $N = 5$ can achieve the case V dispersion with NRMSD $\leqslant 1\%$ using 88 out of 3716 BNN. Furthermore, a consideration of NRMSD $\leqslant 2\%$ reduces the lattice complexity to $N = 3$ where 44 BNN interactions hold normalized stiffness higher than the threshold. In contrast, we find that lattice complexity needs to be greater than 30 to achieve NRMSD $\leqslant 0.1\%$ for case V. We continue the dispersion customization to investigate the lattice complexity when multiple CPs appear in the BZ. Figures 6(c) and 6(d) show a dispersion with 12 maxons, 4 rotons, and 12 saddle points (case VI). In this case, we achieve NRMSD $\leqslant 2\%$ for $N = 5$ and NRMSD $\leqslant 1\%$ for $N = 7$. Advancing the customization of CPs, we include rings of maxon and roton within the first BZ, as shown in Figs. 6(e) and 6(f) (case VII), with the analytical expression

$$\Omega^2(q_x, q_y) = 2 - \cos\left(\sqrt{q_x^2 + q_y^2}\right) - \cos\left(2\sqrt{q_x^2 + q_y^2}\right). \quad (18)$$

Equation (18) has two distinct localized modes: *maxon* ring and *roton* ring, with radii of $\pi/2$ and $\pi$, respectively, highlighted by the yellow circles in Fig. 6(e). We achieve the case VII dispersion with $N = 3$ resulting in an NRMSD $\leqslant 1\%$ using only 44 out of 3716 BNN interactions. Also, a lattice with $N = 13$ gives NRMSD $\leqslant 0.1\%$ to achieve these rings of maxon and roton. We customize a flat band (case VIII) dispersion, which maintains a constant frequency value after reaching a maxon ring localized mode. Analytically, a flat band is expressed as

$$\Omega^2(q_x, q_y) = \begin{cases} q_x^2 + q_y^2 & \text{if } q_x^2 + q_y^2 < \pi^2/4, \\ \pi^2/4 & \text{if } q_x^2 + q_y^2 \geqslant \pi^2/4, \end{cases} \quad (19)$$

which has a maxon ring at $q_x^2 + q_y^2 = \pi^2/4$. The achieved case VIII dispersion's contour is shown in Fig. 6(g) with a three-dimensional (3D) view in Fig. 6(h) where it has a constant frequency of $\omega = \pi/2$ when $q_x^2 + q_y^2 \geqslant \pi^2/4$. We achieve an NRMSD $\leqslant 2\%$ for a lattice size of $N = 5$, requiring only 106 out of 3716 BNN interactions. Furthermore, for $N = 7$, we achieve the case VIII dispersion with NRMSD $\leqslant 1\%$.

For comprehensive clarity, we have tabulated all targets and achieved dispersion relations, their respective lattice complexities for 2%, 1%, and 0.1% NRMSD, in Table I.

For all the cases V–VIII discussed in Fig. 6, we show the error analyses between the target and achieved dispersions in Fig. 7. Here, we also notice that the complex lattices with larger $N$ perform better. If aiming at NRMSD $\leqslant 2\%$, a design with $N = 5$ is sufficient for all the dispersions mentioned in Fig. 6. Our results show that $N \geqslant 13$ confirms NRMSD $\leqslant 0.1\%$ for case VII. In contrast, the case VIII dispersion needs $N \geqslant 28$ to achieve NRMSD $\leqslant 0.1\%$ while the cases V and VI dispersion need $N > 30$ to reduce the NRMSD $\leqslant 0.1\%$. We show more cases with localized mode in Sec. II A of Supplemental Materials [59].

TABLE I. The lattice complexity required to achieve 2%, 1%, and 0.1% NRMSD.

| Target dispersion | Minimum $N$ for NRMSD threshold 2.0% | 1.0% | 0.1% |
|---|---|---|---|
| I. $C_2$ symm, Figs. 2(a),2(b) | 3 | 3 | 3 |
| II. $C_4$ symm, Figs. 2(c),2(d) | 3 | 5 | 22 |
| III. Nearly $C_6$ symm, Figs. 2(e),2(f) | 3 | 4 | 16 |
| IV. Nearly $C_8$ symm, Figs. 2(g),2(h) | 4 | 4 | 12 |
| V. Critical pts, Figs. 6(a),6(b) | 3 | 5 | – |
| VI. Critical pts, Figs. 6(c),6(d) | 5 | 7 | – |
| VII. Critical rings, Figs. 6(e),6(f) | 2 | 3 | 13 |
| VIII. Flat-band, Figs. 6(g),6(h) | 5 | 7 | 28 |
| IX. Aniso.-to-iso., Figs. 8(a),8(b) | 5 | 7 | 22 |
| X. Aniso.-to-iso., Figs. 8(c),8(d) | 3 | 5 | 28 |

## VII. ANISOTROPY-TO-ISOTROPY TRANSITIONS

Lastly, we consider customizing dispersion bands showing transitions from anisotropy-to-isotropy wave behavior. Figures 8(a)–8(b) and 8(c)–8(d) represent achieved dispersion bands of phononic crystal that undergo anisotropy-to-isotropy transitions, showing $C_2$ (case IX) and $C_4$ symmetries (case X), respectively. Cases IX and X dispersion bands are constructed through 2D array of frequency data that form highly noncircular contours at lower wave numbers and transit to perfect circular contours at higher wave numbers.

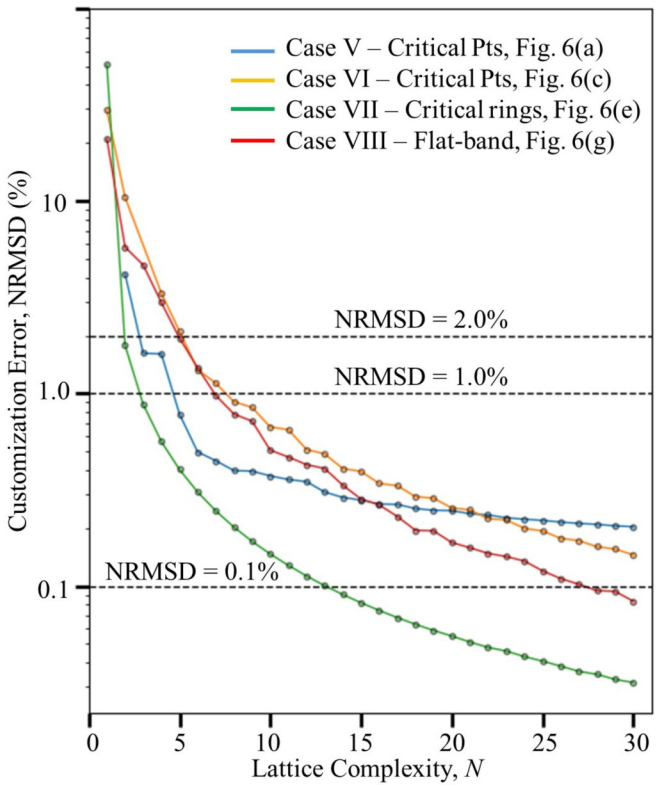


FIG. 7. Error analyses for the Cases V, VI, VII, and VIII dispersion relations shown in Figs. 6(a), 6(c), 6(e), and 6(g), respectively, indicating the lattice complexity needed to achieve 2%, 1% and 0.1%.

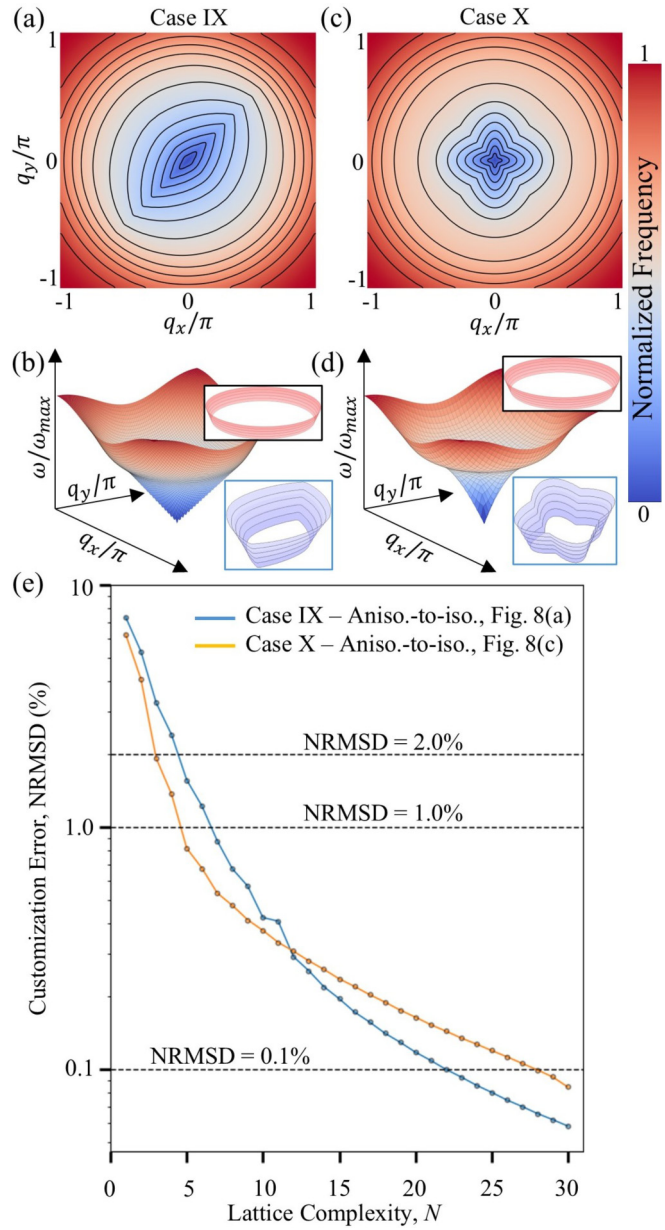


FIG. 8. Dispersion characteristics, showing the transition from anisotropy-to-isotropy within the first BZ for (a) $C_2$ and (c) $C_4$ symmetries, highlighting their pronounced anisotropic behavior as the wave number $(q_x, q_y)$ approaches zero and its transition to isotropy as $(q_x, q_y)$ approaches $\pm\pi$. Here, (b) and (d) show the 3D views of dispersion bands with $C_2$ and $C_4$ symmetries, respectively, with enlarged views. The top and bottom enlarged portions in (b) and (d) highlight the surfaces within the normalized frequency ranges of 0.7-0.8 and 0.3-0.4, respectively. The top portions demonstrate isotropic behavior, while the bottom portions reveal anisotropic behavior, and (e) represents the NRMSD analyses with the lattice complexity.

We evaluate the errors between the target and achieved dispersions using Eq. (12), and Fig. 8(e) provides the error-analysis plots for both cases with anisotropy-to-isotropy transition. For the case IX dispersion in Fig. 8(a), we obtain

NRMSD $\leqslant 2\%$ for $N = 5$, NRMSD $\leqslant 1\%$ for $N = 7$, and NRMSD $\leqslant 0.1\%$ for $N = 22$. The case X dispersion in Fig. 8(c) needs $N = 3$, 5, and 28 to maintain NRMSD $\leqslant$ 2%, 1%, and 0.1%, respectively. We find 160 and 376 out of 3716 BNN interactions are sufficient to keep NRMSD 0.1% for cases IX and X, respectively. We present more anisotropy-to-isotropy transition cases and some exotic dispersion in Secs. II B and II C of Supplemental Materials [59].

## VIII. CONCLUSION

In this theoretical research, we demonstrate the customization of two-dimensional phonon dispersions by the inverse-design approach of nonlocal phononic metamaterials. We show the feasibility of designing phononic crystal lattices to match any valid dispersion bands, whether defined by analytical expressions or arrays of numerical points. We accomplish the design of dispersion bands with multifold rotational symmetry. We also show the possibility of introducing critical points representing localized wave modes. We report the lattice complexities corresponding to different levels of global deviation (NRMSD) in Table I. For all ten cases, the NRMSD less than 2% and 1% can be achieved with $N = 5$ and 7, respectively. We also note that the global NRMSD does not guarantee the existence of critical points (CPs) prescribed in the targets. To achieve the appearance of all CPs at the desirable frequency and wave vector, we need lattices with higher complexity. In addition, our work also demonstrates an unusual anisotropy-to-isotropy transition of dispersion surface while moving from low to high wave numbers. This work points to a new avenue of metamaterial research by customizing wave dispersion properties.

Translating this theoretical research into practical metamaterials presents significant challenges due to the complexity of numerous BNN interactions within the lattice. However, recent advances in metamaterials, particularly involving negative stiffness [63–68] and cubic-symmetry acoustic metamaterials with intricate nonlocal interactions [46,69,70], offer a promising pathway. Additionally, applying machine learning approaches, such as sparsity-promoting optimization [71,72], may help reduce the number of BNN interactions. These developments suggest that additive manufacturing might be a viable method for realizing these complex designs.

The stiffness data for all cases from the inverse design, numerical target dispersion data, and code we use in this study are available in the GitHub repository [73].

## ACKNOWLEDGEMENTS

This research received funding from the Department of Mechanical Engineering at the University of Utah. The work is also partially supported by the National Science Foundation under Grant No. 2341003. The support and resources from the Center for High-Performance Computing at the University of Utah are gratefully acknowledged. The authors are grateful to Professor Srikantha Phani at UBC for thought-provoking discussions.

[1] M. I. Hussein, M. J. Leamy, and M. Ruzzene, Dynamics of phononic materials and structures: Historical origins, recent progress, and future outlook, Appl. Mech. Rev. **66**, 040802 (2014).

[2] T. Vasileiadis, J. Varghese, V. Babacic, J. Gomis-Bresco, D. Navarro Urrios, and B. Graczykowski, Progress and perspectives on phononic crystals, J. Appl. Phys. **129**, 160901 (2021).

[3] M. Nomura, V. Laude, and M. Maldovan, Phononic crystals at various frequencies, APL Mater. **10**, 050401 (2022).

[4] J. Shim, P. Wang, and K. Bertoldi, Harnessing instability-induced pattern transformation to design tunable phononic crystals, Int. J. Solids Struct. **58**, 52 (2015).

[5] N. Aravantinos-Zafiris, N. Kanistras, and M. M. Sigalas, Acoustoelastic phononic metamaterial for isolation of sound and vibrations, J. Appl. Phys. **129**, 105108 (2021).

[6] S. G. Konarski and C. J. Naify, Elastic bandgap widening and switching via spatially varying materials and buckling instabilities, JASA Express Lett. **1**, 015602 (2021).

[7] Q. Wu, P. Shivashankar, X. Xu, Y. Chen, and G. Huang, Engineering nonreciprocal wave dispersion in a nonlocal micropolar metabeam, J. Compos. Mater. **57**, 771 (2023).

[8] M. Alshaqaq, C. Sugino, and A. Erturk, Digital programming of reciprocity breaking in resonant piezoelectric metamaterials, Phys. Rev. Res. **5**, 043003 (2023).

[9] M. N. Hasan, T. E. Greenwood, R. G. Parker, Y. L. Kong, and P. Wang, Fractal patterns in the parameter space of a bistable duffing oscillator, Phys. Rev. E **108**, L022201 (2023).

[10] Y. Wang, J. Lee, and P. X.-L. Feng, Perspectives on phononic waveguides for on-chip classical and quantum transduction, Appl. Phys. Lett. **124**, 070502 (2024).

[11] M. Gattin, N. Bochud, Q. Grossman, D. Ruffoni, G. Rosi, and S. Naili, Ultrasound monitoring of multiphase architectured media: Bandgap tracking via the measurement of the reflection coefficient, Appl. Acoustics **217**, 109844 (2024).

[12] P. Wang, J. Shim, and K. Bertoldi, Effects of geometric and material nonlinearities on tunable band gaps and low-frequency directionality of phononic crystals, Phys. Rev. B **88**, 014304 (2013).

[13] M. Miniaci and R. K. Pal, Design of topological elastic waveguides, J. Appl. Phys. **130**, 141101 (2021).

[14] S. Nair, T. F. Walsh, G. Pickrell, and F. Semperlotti, Physics and geometry informed neural operator network with application to acoustic scattering, arXiv:2406.03407.

[15] M. Kumar and F. Semperlotti, On the geometric phase and its role in the design of elastic topological materials, arXiv:2403.08711.

[16] Z. G. Nicolaou and A. E. Motter, Anharmonic classical time crystals: A coresonance pattern formation mechanism, Phys. Rev. Res. **3**, 023106 (2021).

[17] T. A. Jui and R. K. Pal, Topological localized modes in moiré lattices of bilayer elastic plates with resonators, J. Sound Vib. **576**, 118268 (2024).

[18] M. M. Samak and O. R. Bilal, Evidence of zero group velocity at the lowest dispersion branch through local interactions, APL Mater. **12**, 011111 (2024).

[19] R. L. Thomes, D. Beli, C. Sugino, A. Erturk, and C. D. M. Junior, Programmable moving defect for spatiotemporal wave localization in piezoelectric metamaterials, Phys. Rev. Appl. **19**, 064031 (2023).

[20] Z. G. Nicolaou and J. J. Bramburger, Complex localization mechanisms in networks of coupled oscillators: Two case studies, Chaos **34**, 013131 (2024).

[21] Y. Chen, J. Schneider, K. Wang, P. Scott, S. Kalt, M. Kadic, and M. Wegener, Anomalous frozen evanescent phonons, PREPRINT (Version 1) available at Research Square (2024).

[22] S. C. Paul, H. Oh, J. Hochhalter, and P. Wang, Effects of pore shape contour on band gaps of 2D periodic structures, in *APS March Meeting Abstracts*, APS Meeting Abstracts, Vol. 2023 (2023) p. D09.011.

[23] S. Paul, J. T. B. Overvelde, J. Hochhalter, and P. Wang, Effects of void geometry on two-dimensional monolithic porous phononic crystals, Appl. Phys. Lett. **124**, 212201 (2024).

[24] L. Katch, M. Moghaddaszadeh, C. L. Willey, A. T. Juhl, M. Nouh, and A. P. Argüelles, Analysis of geometric defects in square locally resonant phononic crystals: A comparative study of modeling approachesa), J. Acoust. Soc. Am. **154**, 3052 (2023).

[25] H. B. Al Babaa and M. Nouh, The role of frequency and impedance contrasts in bandgap closing and formation patterns of axially-vibrating phononic crystals, J. Appl. Mech. **91**, 031006 (2024).

[26] S. Han, N. Ma, H. Zheng, Q. Han, and C. Li, Intelligently optimized arch-honeycomb metamaterial with superior bandgap and impact mitigation capacity, Composites Part A: Appl. Sci. Manuf. **185**, 108298 (2024).

[27] C. Chong, B. Kim, E. Wallace, and C. Daraio, Modulation instability and wavenumber bandgap breathers in a time layered phononic lattice, Phys. Rev. Res. **6**, 023045 (2024).

[28] D. Tang, Nonlocality and strength of interatomic interactions inducing the topological phonon phase transition, arXiv:2404.12557.

[29] S. Li, P. G. Kevrekidis, and J. Yang, Emergence of elastic chiral Landau levels and snake states, Phys. Rev. B **109**, 184109 (2024).

[30] A. S. Phani, J. Woodhouse, and N. A. Fleck, Wave propagation in two-dimensional periodic lattices, J. Acoust. Soc. Am. **119**, 1995 (2006).

[31] M. J. Leamy, Exact wave-based bloch analysis procedure for investigating wave propagation in two-dimensional periodic lattices, J. Sound Vib. **331**, 1580 (2012).

[32] A. Kazemi, K. J. Deshmukh, F. Chen, Y. Liu, B. Deng, H. C. Fu, and P. Wang, Drawing dispersion curves: Band structure customization via nonlocal phononic crystals, Phys. Rev. Lett. **131**, 176101 (2023).

[33] C. Choi, S. Bansal, N. Münzenrieder, and S. Subramanian, Fabricating and assembling acoustic metamaterials and phononic crystals, Adv. Eng. Mater. **23**, 2000988 (2021).

[34] S.-H. Jo and B. D. Youn, An explicit solution for the design of a target-frequency-customized, piezoelectric-defect-introduced phononic crystal for elastic wave energy harvesting, J. Appl. Phys. **130**, 184902 (2021).

[35] R. Fleury, Non-local oddities, Nat. Phys. **17**, 766 (2021).

[36] M. I. N. Rosa and M. Ruzzene, Dynamics and topology of non-hermitian elastic lattices with non-local feedback control interactions, New J. Phys. **22**, 053004 (2020).

[37] A. Martowicz, M. Ruzzene, W. J. Staszewski, J. J. Rimoli, and T. Uhl, Out-of-plane elastic waves in 2d models of solids: A case study for a nonlocal discretization scheme with reduced numerical dispersion, Math. Probl. Eng. **2015**, 584081 (2015).

[38] A. Rajabpoor Alisepahi, S. Sarkar, K. Sun, and J. Ma, Breakdown of conventional winding number calculation in one-dimensional lattices with interactions beyond nearest neighbors, Commun. Phys. **6**, 334 (2023).

[39] Y. Chen, M. A. A. Abouelatta, K. Wang, M. Kadic, and M. Wegener, Nonlocal cable-network metamaterials, Adv. Mater. **35**, 2209988 (2023).

[40] M. I. N. Rosa and M. Ruzzene, Small-world disordered lattices: Spectral gaps and diffusive transport, New J. Phys. **24**, 073020 (2022).

[41] F. Farzbod and M. J. Leamy, Analysis of Bloch's method and the propagation technique in periodic structures, J. Vib. Acoust. **133**, 031010 (2011).

[42] P. Zhang, Y. Liu, K. Zhang, Y. Wu, F. Chen, Y. Chen, P. Wang, and X. Zhu, Observation of maxon-like ultrasound in elastic metabeam, APL Mater. **12**, 031110 (2024).

[43] Y. Chen, M. Kadic, and M. Wegener, Roton-like acoustical dispersion relations in 3d metamaterials, Nat. Commun. **12**, 3278 (2021).

[44] Z. Duan, J. Cui, L.-Q. Chen, and T. Yang, Nonlinear mechanical roton, J. Appl. Mech. **90**, 031010 (2023).

[45] Y. Chen, J. L. G. Schneider, M. F. Groß, K. Wang, S. Kalt, P. Scott, M. Kadic, and M. Wegener, Observation of chirality-induced roton-like dispersion in a 3d micropolar elastic metamaterial, Adv. Funct. Mater. **34**, 2302699 (2024).

[46] K. Wang, Y. Chen, M. Kadic, C. Wang, and M. Wegener, Nonlocal interaction engineering of 2d roton-like dispersion relations in acoustic and mechanical metamaterials, Commun. Mater. **3**, 35 (2022).

[47] J.-G. Cui, T. Yang, M.-Q. Niu, and L.-Q. Chen, Tunable roton-like dispersion relation with parametric excitations, J. Appl. Mech. **89**, 111005 (2022).

[48] Z. Zhu, Z. Gao, G.-G. Liu, Y. Ge, Y. Wang, X. Xi, B. Yan, F. Chen, P. P. Shum, H. X. Sun, and Y. Yang, Observation of multiple rotons and multidirectional roton-like dispersion relations in acoustic metamaterials, New J. Phys. **24**, 123019 (2022).

[49] A. Banerjee, K. K. Bera, and S. Adhikari, Enhanced damping and bandwidth in roton-like dispersion of a beyond nearest neighbour periodic chain, Available at SSRN 4766229 (2023).

[50] T. Lawrie, G. Tanner, and G. Chaplain, Engineering metamaterial interface scattering coefficients via quantum graph theory, Acta Phys. Pol. A **144**, 486 (2023).

[51] A. Bossart and R. Fleury, Extreme spatial dispersion in non-locally resonant elastic metamaterials, Phys. Rev. Lett. **130**, 207201 (2023).

[52] I. Arretche and K. H. Matlack, Effective phononic crystals for non-cartesian elastic wave propagation, Phys. Rev. B **102**, 134308 (2020).

[53] W. Li and W. Chen, Simulation of the band structure for scalar waves in 2d phononic crystals by the singular boundary method, Engineering Analysis with Boundary Elements **101**, 17 (2019).

[54] M. Attarzadeh and M. Nouh, Non-reciprocal elastic wave propagation in 2d phononic membranes with spatiotemporally varying material properties, J. Sound Vib. **422**, 264 (2018).

[55] Q. Ni and J. Cheng, Anisotropy of effective velocity for elastic wave propagation in two-dimensional phononic crystals at low frequencies, Phys. Rev. B **72**, 014305 (2005).

[56] S.-C. S. Lin and T. J. Huang, Tunable phononic crystals with anisotropic inclusions, Phys. Rev. B **83**, 174303 (2011).

[57] Y. Chen, M. Kadic, and M. Wegener, Chiral triclinic metamaterial crystals supporting isotropic acoustical activity and isotropic chiral phonons, Proc. R. Soc. London A **477**, 20200764 (2021).

[58] V. N. Gorshkov, N. Navadeh, and A. S. Fallah, A study of frequency band structure in two-dimensional homogeneous anisotropic phononic k3-metamaterials, Smart Mater. Struct. **26**, 095058 (2017).

[59] See Supplemental Material at http://link.aps.org/supplemental/10.1103/PhysRevB.110.144304 for a detailed derivation of the dispersion relation of a 2D square lattice, the conditions for a valid target dispersion band, the inverse design procedure using the Fourier series approach, the error calculation between the target and achieved dispersion bands, the generation of a 2D array of frequency data as a target function, and additional cases of dispersion customization, including localized modes, anisotropy-to-isotropy transitions, and other exotic features.

[60] J. D. Joannopoulos, S. G. Johnson, J. N. Winn, and R. D. Meade, *Photonic Crystals: Molding the Flow of Light*, 2nd ed. (Princeton University Press, Princeton, 2008).

[61] N. F. Q. Yuan and L. Fu, Classification of Critical points in energy bands based on topology, scaling, and symmetry, Phys. Rev. B **101**, 125120 (2020).

[62] A. Chandrasekaran, A. Shtyk, J. J. Betouras, and C. Chamon, Catastrophe theory classification of Fermi surface topological transitions in two dimensions, Phys. Rev. Res. **2**, 013355 (2020).

[63] Z. G. Nicolaou and A. E. Motter, Mechanical metamaterials with negative compressibility transitions, Nat. Mater. **11**, 608 (2012).

[64] B. M. Goldsberry and M. R. Haberman, Negative stiffness honeycombs as tunable elastic metamaterials, J. Appl. Phys. **123**, 091711 (2018).

[65] S. Zhu, B. Wang, X. Tan, J. Hu, L. Wang, Z. Zhou, and S. Chen, A novel bi-material negative stiffness metamaterial in sleeve-type via combining rigidity with softness, Comp. Struct. **262**, 113381 (2021).

[66] X. Tan, S. Chen, B. Wang, J. Tang, L. Wang, S. Zhu, K. Yao, and P. Xu, Real-time tunable negative stiffness mechanical metamaterial, Extreme Mech. Lett. **41**, 100990 (2020).

[67] T. Klatt and M. R. Haberman, A nonlinear negative stiffness metamaterial unit cell and small-on-large multiscale material model, J. Appl. Phys. **114**, 033503 (2013).

[68] X. Tan, B. Wang, S. Zhu, S. Chen, K. Yao, P. Xu, L. Wu, and Y. Sun, Novel multidirectional negative stiffness mechanical metamaterials, Smart Mater. Struct. **29**, 015037 (2020).

[69] K. Wang, Y. Chen, M. Kadic, C. Wang, and M. Wegener, Cubic-symmetry acoustic metamaterials with roton-like dispersion relations, Acta Mech. Sinica **39**, 723020 (2023).

[70] Y. Chen, K. Wang, M. Kadic, S. Guenneau, C. Wang, and M. Wegener, Phonon transmission through a nonlocal metamaterial slab, Commun. Phys. **6**, 75 (2023).

[71] Z. G. Nicolaou, G. Huo, Y. Chen, S. L. Brunton, and J. N. Kutz, Data-driven discovery and extrapolation of parameterized pattern-forming dynamics, Phys. Rev. Res. **5**, L042017 (2023).

[72] S. L. Brunton, J. L. Proctor, and J. N. Kutz, Discovering governing equations from data by sparse identification of nonlinear dynamical systems, Proc. Natl. Acad. Sci. **113**, 3932 (2016).

[73] https://github.com/Sharat1214019/2D_PC_single_band_customization.git.